

Influence of Mn on the Corrosion Behaviour of Medium Manganese Steels in a Simulated Seawater Environment

Guanqiao Su, Xiuhua Gao^{}, Linxiu Du, Dazheng Zhang, Jun Hu, Zhenguang Liu*

The State Key Laboratory of Rolling and Automation, Northeastern University, Shenyang 110819, Liaoning, P.R.China.

*E-mail: suhang_joe@163.com

Received: 13 August 2016 / *Accepted:* 18 September 2016 / *Published:* 10 October 2016

The influence of Mn on the corrosion behaviour of medium manganese steels was studied by employing a laboratory accelerated corrosion test that involved cyclic wet/dry conditions in a simulated seawater environment. At different time points during the cyclic corrosion tests, the character of the rust film and the susceptibility of the tested medium manganese steels to corrosion were examined using SEM, XRD, and EPMA as well as analysis of the potential-pH diagram. The medium manganese steels exhibited lower corrosion resistance due to the enrichment of MnFe_2O_4 in the rust films. Moreover, the effect of small amounts of alloying Mo and Ni elements on medium manganese steels was discussed.

Keywords: medium manganese steel; weight loss; SEM; Pourbaix diagram; rust

1. INTRODUCTION

Because of its high strength, substantial toughness at low temperature, and excellent ductility, medium manganese (Mn) steel has great potential to replace its traditional low-strength counterpart for infrastructure in seawater environments. Use of it dominates in marine steel applications, including offshore structures, ship construction, and steel bridges in coastal environments. However, the medium-Mn steel surface is adversely affected by the harsh marine environment; therefore, its corrosion behavior must be studied. The various chemical elements available (such as nickel, chromium, silicon and copper) have the potential to play a significant part in application of marine steel, and the characterization of such steel suggests its corrosion resistance is due to the enrichment of oxides of these elements in the rust films [1,2]. More importantly, chemical elements can further the accumulation of rust films, which become serried over time in a gradual manner and weaken the

function of some marine agents, resulting in substantial diminution of the corrosion rate [3-8]. The formation of adherent and colored films on the steel matrix was readily noticed [9,10]. Unquestionably, the elemental content of steel impacts the precipitation of corrosion products. Y.H. Qian et al. [11] found that chromium effectively reduces the corrosion sensitivity of various Cr-containing steels in an industrial environment, and a higher proportion of elemental chromium could improve this effect. Chromium oxides or hydroxides are conducive to the accumulation of a dense film near the inner area of the rust, which plays a corrosion medium-resistant barrier and decreases the anodic dissolution of the matrix. Diaz et al. [12] found that the enrichment of nickel in steel improves the proportion of nanophasic or superparamagnetic α -FeOOH (the size of the particle is less than 15 nm) near the inner area of the rust film and increases its tightness and resistance to corrosion in marine atmospheres. In addition, a silicon content in steels of approximately 2% was reported to contribute to the corrosion resistance of low alloy steels [7,13]. Many authors have reported alloy elements in steel may either exhibit synergy with each other or adversely affect each other. Bousselmi [14] and Choi and Kim [15] studied chromium co-existed copper and found they had a synergistically beneficial role in the corrosion process of mild steel. The presence of copper can notably weak the corrosion kinetics curve of weathering steels, and the combination of chromium with copper presents a synergistically enhancing effect on the corrosion process. B.W. Forgeson [16] and W.A. Schultze [17] found that copper and chromium were detrimental for long-term corrosion. L. Hao et al. [18] identified elemental Mn and Cu in bivalent and univalent cations in Fe_3O_4 crystal, respectively, and this phenomenon may reduce anion selectivity of the rust film in a simulated atmospheric environment.

No studies on the influence of manganese on the corrosion behaviour of medium manganese steel have been found thus far. This work clarifies the role of manganese in the corrosion process through the cyclic wet/dry corrosion test (a simulated seawater environment).

2. EXPERIMENTAL

2.1 Materials

Two types of medium manganese steels were melted using a vacuum induction furnace. After adding the alloy elements, the steel was cast into ingots and forged into 140 mm thick billets. The billets were homogenized at 1200 °C for 1 h then rolled into 30 mm thick plates at 960 °C in 11 passes and quenched with water to room temperature. Finally, the plates were reheated to 650 °C for 100 min and air-cooled to room temperature. The chemical compositions of the medium manganese steels tested in this work are given in Table 1.

Table 1. Chemical compositions of the specimens (in mass %).

Sample	C	Si	Mn	P	S	Al	Mo	Ni	Fe
Mn-Mo	0.1	0.2	5.0	0.003	0.001	0.01	0.42	-	Balance
Mn-Mo-Ni	0.04	0.2	5.5	0.003	0.001	0.01	0.22	0.30	Balance

The yield strength and ultimate tensile strength of the tested Mn-Mo steel are 740MPa and 856MPa, respectively, and the elongation-to-failure and shrinkage rate of the tested Mn-Mo steel are 32.5% and 70.9%, respectively. For the tested Mn-Mo-Ni steel, the yield strength, ultimate tensile strength, elongation-to-failure rate and shrinkage rate were 685MPa, 806MPa, 27.3% and 70.5%, respectively.

2.2 Accelerated corrosion test of medium Mn Steel

The tested steel coupons were cut from the plate along the rolling direction into 60 mm × 40 mm × 4 mm and 20 mm × 15 mm × 4 mm pieces. Then, the coupons were cleaned with petroleum ether, alcohol and acetone using an ultrasonic cleaner and dried with clean air at room temperature. The weight of the coupons (60 mm × 40 mm × 4 mm) was measured using a balance (0.1 mg precision) for weight loss measurements. A 3-mm diameter hole was machined into the coupons to hang them in the corrosion experiment box by non-metallic wires. Finally, the surface of the coupons was burnished by 200, 400, 600, 800, 1200 grit silicon carbide sand paper.

According to the EN ISO 11130 standard, a cyclic wet/dry corrosion test was carried out in a simulated seawater solution at 25 °C. The mixed solution was prepared from 90 L of deionized water and contained 3.5 mass% analytical-grade NaCl. The pH of the solution was adjusted with NaOH to 6.5. Each corrosion cycle consisted of a drying period plus a wetting period, and their durations were set as 50 minutes and 10 minutes, respectively. The corrosion time of the cyclic corrosion test was divided into six periods: 24 hours, 72 hours, 168 hours, 288 hours, 432 hours, and 600 hours. The humidity in the corrosion experiment equipment was maintained at 45% by deionized water atomization.

After the cyclic corrosion test, the rust films were removed from the larger coupons. The coupons were scraped by a wire brush to shave the loose rust layer from the surface and then immersed in a mixture of 100 mL of hydrochloric acid (37 vol.%) and 10 g of hexamethylenetetramine (urotropine) in 900 mL of distilled water. Finally, the coupons were rinsed in acetone and alcohol and dried by cool air. After removing the corrosion products, the coupons were measured again to calculate the corrosion rate. The corrosion rate is calculated using the weight loss according to the following equation (ASTM standard [19]):

$$\text{Corrosion rate} \left(\frac{\text{mm}}{\text{y}} \right) = \frac{K \times \Delta W}{A \times T \times D} \quad (1)$$

Where $K = 87600$, a constant for corrosion rate evaluated in mm/y, ΔW is weight loss in g, A is the total corrosive area in cm^2 , T is the exposure time in hours, D is the density of the tested medium steel in g/cm^3 .

2.3 Morphology observation and analysis

The corrosion products of the coupons at different corrosion times were observed by a FEI QUANTA 600 scanning electron microscope (SEM). The detection of the corrosion phases was carried out with a D/max-2400 X-ray diffractometer (XRD) with Cu $K\alpha$ ($\lambda = 0.154 \text{ nm}$) target. XRD

analysis was performed in the range of 10 to 70°, and the peak positions of the corrosion phases were identified using MDI Jade software. For EPMA studies, the coupons were set in epoxy, polished by alcohol to achieve a surface roughness of 2.5 µm, and then dried with cool air and stored in a desiccator. The JEOL-8530F electron probe analyser (EPMA) was set to 20 kV voltage and an 11 mm working distance. Backscattered electron scanning along the rust film determined the distribution of alloy elements using EDX line analysis. A CS 300 electrochemical workstation was used to test the potentiodynamic polarization curves of medium Mn steel in the accelerated stage of the whole corrosion process. The corroded steel couple act as working electrode, a Hg/HgCl₂ (SCE) electrode and a platinum sheet serve as reference part and counterpart in the system. The scope of the polarization potential was -0.4 V to 0.4 V vs. SCE, and the speed of potentiodynamic scanning was 0.5 mV/s. The filling of the polarization curves was determined by CView 2 software.

3. RESULTS AND DISCUSSION

3.1 Corrosion rates determined from weight loss measurements

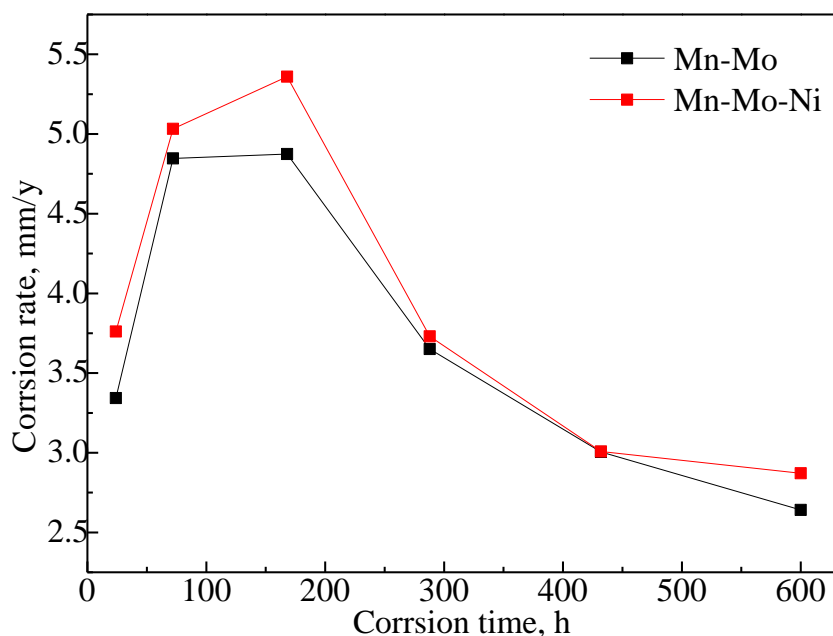


Figure 1. Corrosion kinetics curves of the tested medium manganese steels after different corrosion times in simulated seawater at 25 °C. Each corrosion cycle consisted of a 10 mins wetting period in 3.5 (mass. %) NaCl solution plus a 50 mins drying period.

The corrosion rates according to the weight loss measurements are shown in Fig. 1. The overall trend of the corrosion curves was similar. As shown in Fig. 1, the corrosion process occurred in three stages: an accelerated corrosion stage, a decelerated corrosion stage, and a stable corrosion stage. Fig. 1 also shows that the two types of medium manganese steel have different corrosion resistance; the Mn-Mo-Ni steel had worse corrosion resistance than the Mn-Mo steel due to its higher Mn content.

3.2 Scanning electron microscopy characterization of the corrosion products films

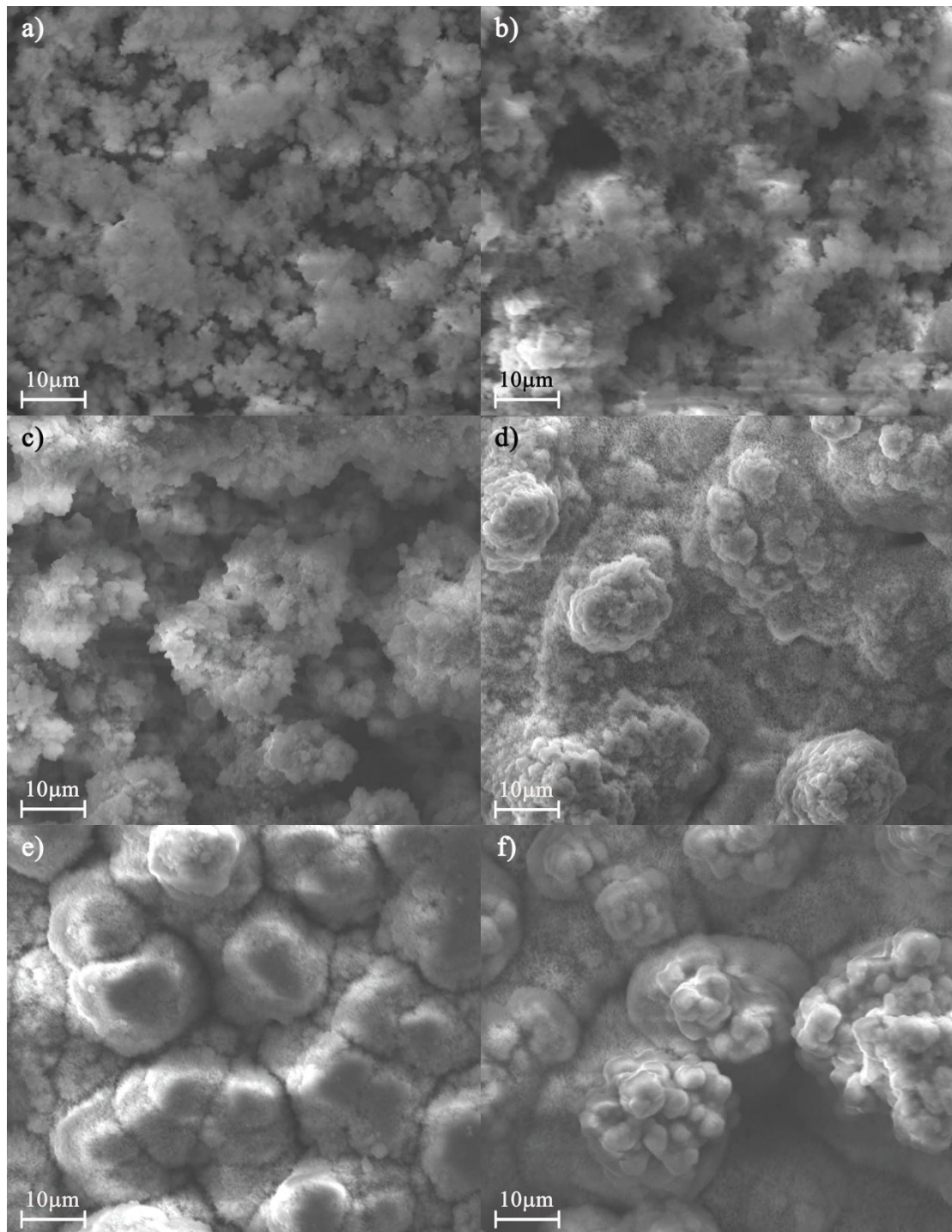


Figure 2. SEM morphologies of corrosion products of Mn-Mo alloy steel after the cyclic corrosion test in simulated seawater at 25 °C: (a) 24 hours; (b) 72 hours; (c) 168 hours; (d) 288 hours; (e) 432 hours; (f) 600 hours.

Fig. 2 shows SEM images of the macrostructure of the Mn-Mo alloy steel at different time points of the cyclic corrosion test in simulated seawater at 25 °C. The rust films formed at all cyclic

corrosion time points were quite nonuniform. The morphology of the rust usually presented in a featureless form, and obvious cracking phenomena did not appear on the couple surface.

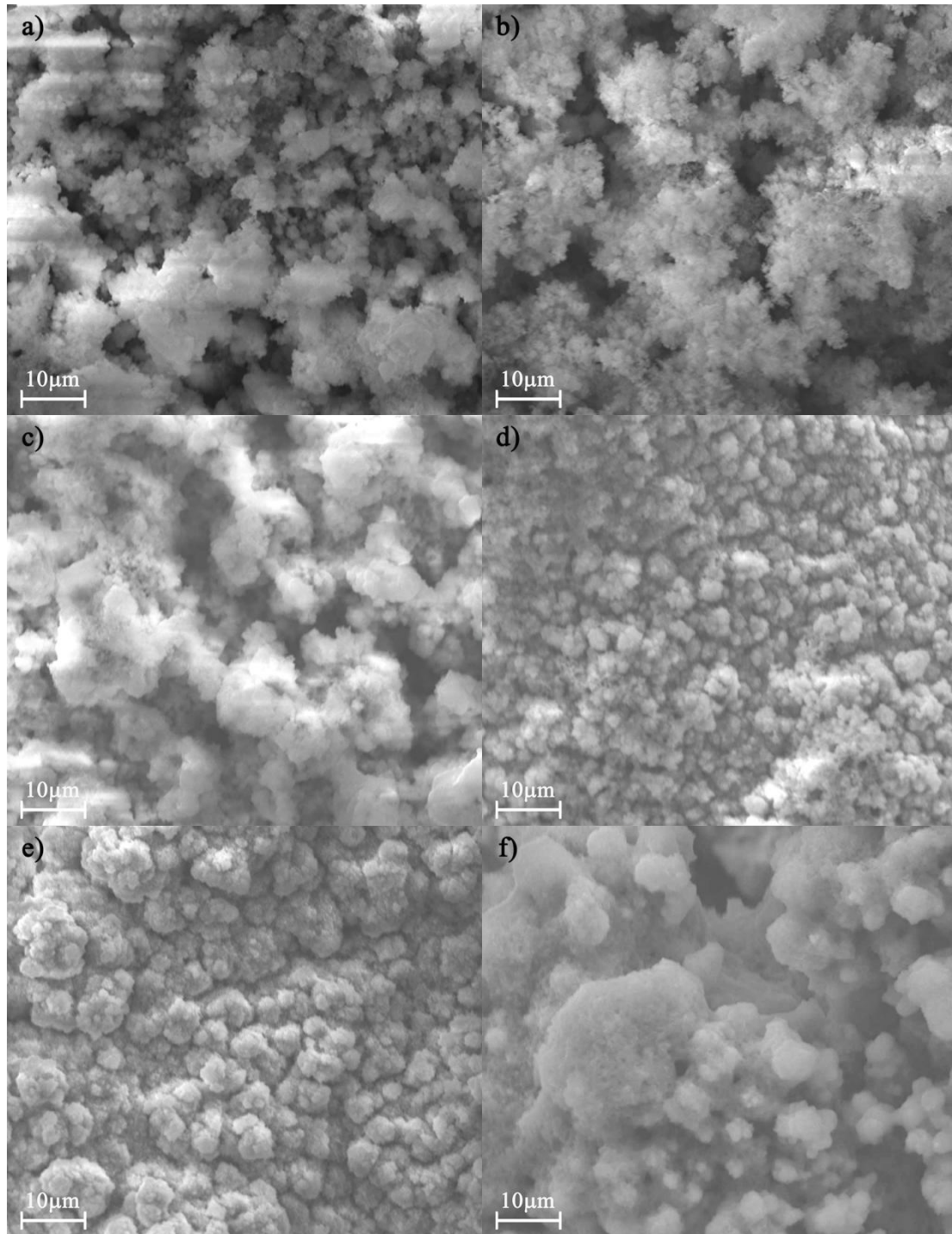


Figure 3. SEM morphologies of corrosion products of Mn-Mo-Ni alloy steel after the cyclic corrosion test in simulated seawater at 25 °C: (a) 24 hours; (b) 72 hours; (c) 168 hours; (d) 288 hours; (e) 432 hours; (d) 600 hours.

Fig. 2a shows that some small shallow crevices on the surface of the tested Mn-Mo steel were blanketed with fine corrosion products. Crevices existing among these initial corrosion products can

act as transmission channels for corrosion solution and oxygen. The featureless and compact areas on the coupons had the typical morphology of $\text{Fe}_{3-x}\text{O}_4$ [20,21,22]. Around the featureless regions, some shorter, flaky structures were observed along the borders. This structure was typical of $\gamma\text{-FeOOH}$ morphology [23]; $\gamma\text{-FeOOH}$ has a loose porous structure that provides a channel for Cl ions to contact the matrix, thus accelerating the electrochemical reaction process. As seen in Fig. 2b and Fig. 2c, the compact, featureless $\text{Fe}_{3-x}\text{O}_4$ of the rust was spalled, and the flaky structure grew upwards. However, the rust presented a loose porous morphology. After 288 hours of corrosion, the surface was covered with a whiskers region by some nodules approximately 5-10 μm in size (Fig. 2d). The morphology of these nodules was of the flaky accumulation form, consisting of the growing $\gamma\text{-FeOOH}$ and the early initiating $\alpha\text{-FeOOH}$. $\alpha\text{-FeOOH}$ gradually appeared at the porous regions of the compact $\text{Fe}_{3-x}\text{O}_4$ rust film. It is possible the initial $\alpha\text{-FeOOH}$ appeared among the porous gaps as a result of the transmutation of $\text{Fe}_{3-x}\text{O}_4$ to $\alpha\text{-FeOOH}$ [25]. Over time, the rust became increasingly dense; the size of the growing $\gamma\text{-FeOOH}$ reached 10 μm and presented with a flat hill morphology (Fig. 2e). As shown in Fig. 2f, the surface morphology presented as a globular (“cotton balls”) morphology, which is a characteristic morphology of $\alpha\text{-FeOOH}$ and develops from whiskers of $\alpha\text{-FeOOH}$ at the cracked edge [21,22,24]. The continuous change of $\alpha\text{-FeOOH}$ from “whiskers” to “cotton balls” results in a relatively stable corrosion rate in the tested steel.

The SEM morphologies of the Mn-Mo-Ni alloy steel after different corrosion times are pictured in Fig. 3. The transformation process of the corrosion products was similar to the Mn-Mo alloy steel, but the appearance of globular (“cotton balls”) $\alpha\text{-FeOOH}$ was not obvious. Compared to the Mn-Mo steel, the morphology of the $\gamma\text{-FeOOH}$ flaky structures were different in terms of size and flat hill morphology of the deposition. After 288 hours of corrosion time, the surface of the coupon was covered with a compact oxide scale overgrown by small nodules approximately 2-3 μm in size (Fig. 3d).

3.3 X-ray diffraction

Fig. 4 presents the XRD patterns of the corrosive products taken from the surface of the two tested steels after corrosion tests of various durations. The corrosion phases of the Mn-Mo steel are presented in Fig. 4a. Corrosion products in the crystallization gradually became stronger and formed on the steel matrix. After a 24 hour corrosion time, the main components of the corrosion phases were lepidocrocite ($\gamma\text{-FeOOH}$), $\text{Fe}_{3-x}\text{O}_4$, a small quantity of Mn_xO_y and steel matrix. During the next corrosion cycles, goethite ($\alpha\text{-FeOOH}$) and some $(\text{Fe,Mn})_x\text{O}_y$ corrosion products appeared in the composition of the rust films. After 432 hours of corrosion time, the proportions of the $(\text{Fe,Mn})_x\text{O}_y$ corrosion phases declined, while the counterpart Mn_xO_y phases rose. Unlike Mn-Mo alloy steel, goethite ($\alpha\text{-FeOOH}$) did not appear in Mn-Mo-Ni alloy steel until 168 hours (Fig. 4b) and the proportions of Mn_xO_y and $(\text{Fe,Mn})_x\text{O}_y$ phases in the rust film surface increased.

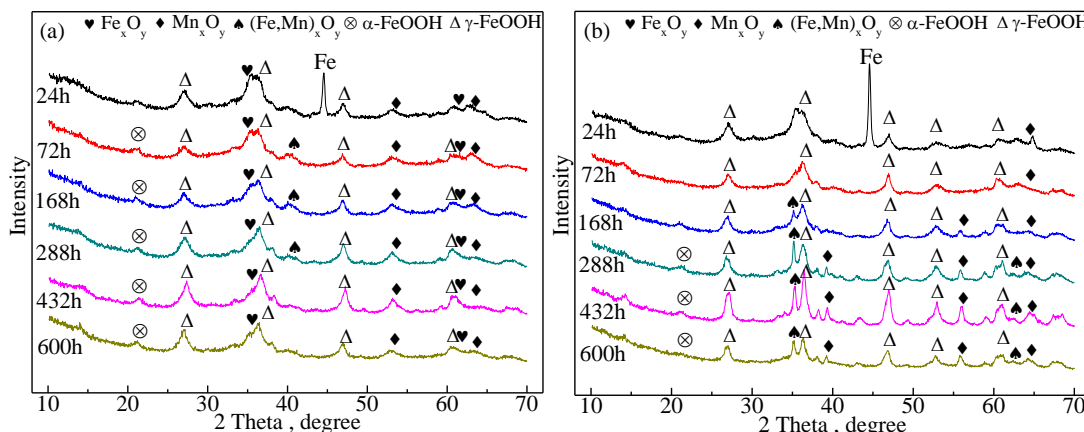
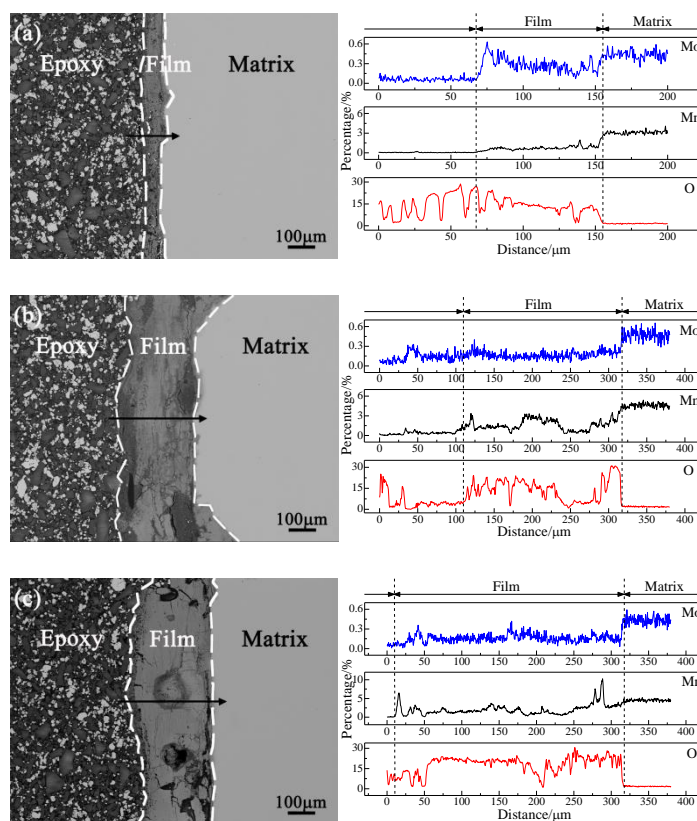


Figure 4. XRD patterns of the tested medium manganese steels after different corrosion times in simulated seawater at 25 °C: (a) Mn-Mo steel; (b) Mn-Mo-Ni steel. Each corrosion cycle consisted of a 10 mins wetting period in 3.5 (mass. %) NaCl solution plus a 50 mins drying period.

3.4 Characterization of the cross section morphologies of corrosion products films

The cross section micrograph and the elemental distribution of the Mn-Mo steel rust film is shown in Fig. 5. The corrosion films covering the steel matrices at each corrosion cycle were well-distributed and increased gradually. The percentage of each alloy element across the rust film at different corrosion times was determined by the corresponding EDX line scanning analysis.



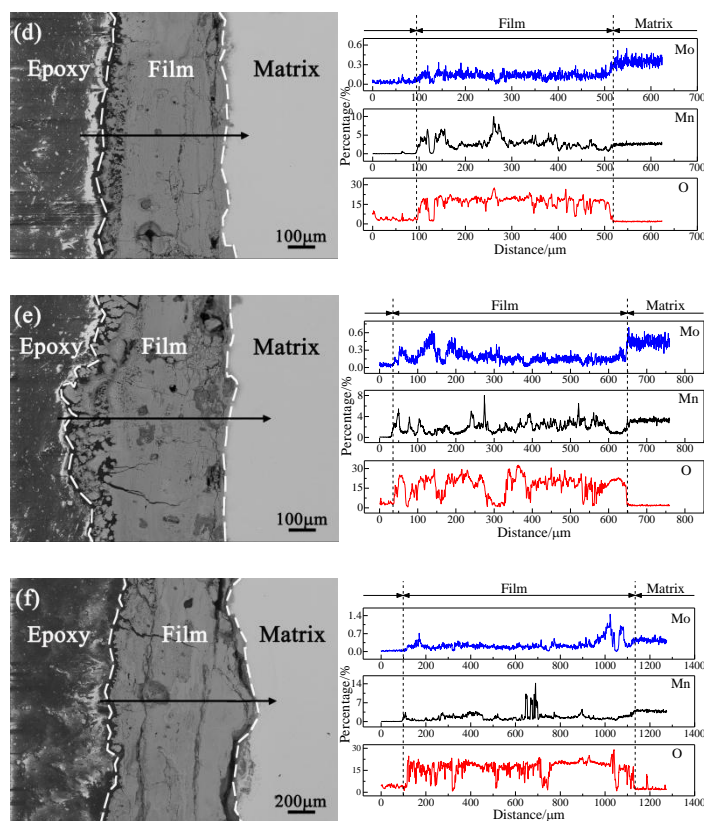


Figure 5. Cross section of the Mn-Mo steel and the main element distribution in the corrosion products films in a simulated seawater environment at 25 °C for different lengths of time: (a) 24 h; (b) 72 h; (c)168 h; (d) 288 h; (e) 432 h; (f) 600 h. Each corrosion cycle consisted of a 10 mins wetting period in 3.5 (mass. %) NaCl solution plus a 50 mins drying period.

The percentage of elemental Mo across the Mn-Mo steel corrosion films changed significantly over different corrosion times, and similar changes in elemental Mn also occurred. However, the area of the element enrichment varied in different corrosion times, and the degree of fluctuation in Mn content is more evident than that of Mo. The enrichment range of the elemental Mo in the Mn-Mo steel rust film at the 24 h corrosion time point appeared near the outer layer. In the following three cycles, Mo did not appear to have an obvious enrichment area. After 432 h of corrosion, Mo was again enriched in the outer layer. In the last cycle, enrichment of Mo peaked, stabilizing the corrosion rate. From line analysis of elemental Mn (Fig. 5), the enrichment phenomenon of Mn was observed to begin in the second cycle but stabilized in the last cycle in only the middle region of the film. It is hypothesized that the instability of Mn concentration in the film may produce certain negative effects on corrosion resistance in steel.

Relative to the Mn-Mo steel, the corrosion film of the Mn-Mo-Ni steel was clearly enriched near the outer film after the first cycle, but Mo was not enriched. Enrichment of the alloy elements Mo and Ni appeared near the inner film after the second cycle. The distribution of the Mn in the five cycles was similar to the Mn-Mo steel except at 24 h (Fig. 8). Adding small amounts of the corrosion resistance elements Mo and Ni do not improve the accelerated corrosion behaviour of Mn.

3.5 Potentiodynamic polarization curves of accelerated corrosion stage

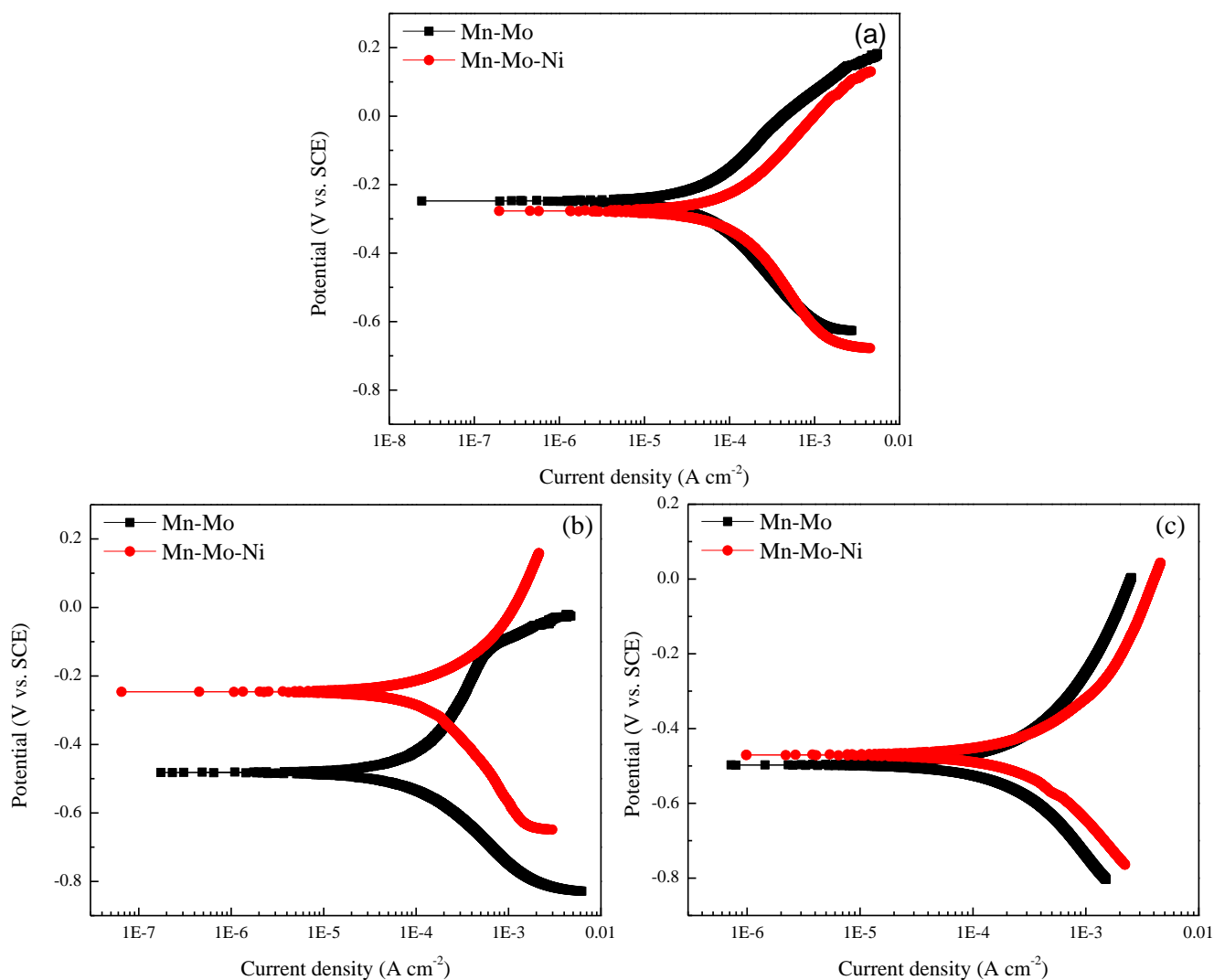


Figure 6. Potentiodynamic polarization curves of couples in 3.5 % NaCl solution with corroded rust films for different lengths of corrosion time: (a) 24 hours; (b) 72 hours; (c) 168 hours.

Potentiodynamic polarization was determined on the two tested medium manganese steels with some corroded couples after the accelerated corrosion stage for different lengths of time. Fig.6 presents the polarization curves determined for the three corrosion cycles of couples in the 3.5% NaCl solution at 25 °C. In every corresponding corrosion period of the two tested medium manganese steel, the degree of accelerating corrosion increases, but no passivation membrane. The electrochemical corrosion parameters (E_{corr} , I_{corr} , b_a , b_c) are given in Table 2. Table 2 presents that, for the two types of medium manganese steel couple in different cycles, the anodic and cathodic Tafel constants (b_a and b_c , respectively) obviously change their values, which indicates a different mechanism for the corrosion reaction of the two types of steels in the simulated seawater [26]. Mn-Mo steel have a small I_{corr} than Mn-Mo-Ni steel in every accelerated cycle. The elemental Mn act as a negative role during the corrosion process. The results from Potentiodynamic polarization curves accord with the corrosion kinetics curves.

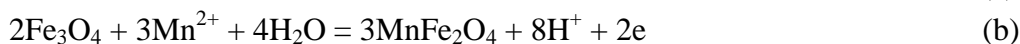
Table 2. Electrochemical corrosion parameters of couples in 3.5 (mass. %) NaCl solution at 25 °C for different lengths of corrosion time by Cview 2 software.

Specimen	E_{corr} (V vs. SCE)	I_{corr} (mA cm ⁻²)	b_a (mV/dec)	$-b_c$ (mV/dec)
Mn-Mo-24h	-0.248	0.0645	302	308
Mn-Mo-Ni-24h	-0.277	0.1528	345	430
Mn-Mo-72 h	-0.482	0.1212	443	272
Mn-Mo-Ni-72h	-0.246	0.2323	282	626
Mn-Mo-168h	-0.497	0.3278	436	438
Mn-Mo-Ni-168h	-0.471	0.4039	326	391

3.6 Corrosion process

From the observed surface morphology and the elemental distribution of the cross section morphology, it can be inferred that the addition of Mn can decrease the corrosion resistance of medium manganese steels. This phenomenon is due to participation of (Fe,Mn)_xO_y in an electrochemical reaction during the corrosion process [27-33]. However, the extent of corrosion varied between the two types of steel with differing Mn content. In the first stages of the corrosion process of the two types of medium manganese steel, anodic and cathodic reactions occurred on the surface due to the presence of Cl⁻ [34].

A potential-pH diagram can determine the stability of the compounds in the corrosion process. The chemical conversion equilibria in the corrosion process for the stable region involved Mn ions and are listed in the following equations (a-c) [18,36,37] :



In the corrosion process, the FeOOH produced by the anodic reaction of Fe may react with Mn²⁺ to generate MnFe₂O₄ [18]. Comparing the distribution of the two elements in the rust films (Fig. 5) illuminates the corrosion behaviour of Mn-Mo steel. Elemental Mn did not appear during the first cycle but appeared during the second cycle. Only the alloy element Mo was enriched near the outer layer of the rust. However, from the elemental distribution of the Mn-Mo-Ni steel rust layer, we found only elemental Mn was enriched near the outer layer. The above phenomena are explained by the preferential transformation of Mo to MoO₄²⁻ on the rust film surface. MoO₄²⁻ will be absorbed on the matrix surface and react with Fe²⁺ ions to generate insoluble FeMoO₄, which will then be deposited on the surface of the matrix. This will prevent corrosive Cl⁻ ions from migrating to the surface. The adsorption of MoO₄²⁻ can hydrate oxide film precipitated from anion permeation, causing cation selective permeability, thus inhibiting corrosion in the early stages of the corrosion process [7,34].

Fig. 7 shows the potential-pH diagrams for the Fe-Mn-H₂O system involving the stable region of MnFe₂O₄ and Fe₃O₄ at 298.15K (by HSC 6.0). The stable regions for Fe₃O₄ and MnFe₂O₄ are separated in the diagram by solid black and blue lines, respectively. The dashed lines represent oxygen and hydrogen equilibria at 1.01 × 10⁵ Pa. The concentrations of the cations and anions in the system

were deemed to be $10^{-6.5}$ mol L⁻¹. In the area of the diagram where MnFe₂O₄ and Fe₃O₄ overlap, these corrosive transform compounds may coexist in a fraction of the area.

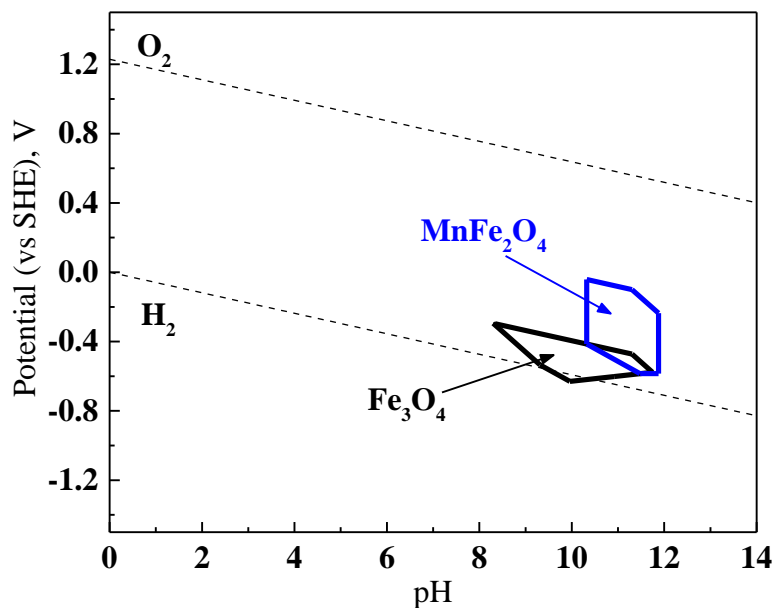


Figure 7. Potential-pH diagram for the Fe-Mn-H₂O system involving MnFe₂O₄ and Fe₃O₄ at 298.15K. The dashed lines represent oxygen and hydrogen equilibria at 1.01×10^5 Pa. The concentrations of the cations and anions in the system are deemed to be $10^{-6.5}$ mol L⁻¹.

The corrosion product Fe₃O₄ has a reverse spinel structure, and Mn(II) can be involved in its formation during the corrosion [18]. In the Mn-Mo steel corrosion process, corrosion films formed in the presence of Cl⁻ ions due to the condensation of dissolved oxygen on the matrix. Once the dissolved oxygen diffuses onto the steel substrate surface, the steel will be oxidized at the anode, and Fe(II) will be dissolved in the steel. So, the corrosion phenomenon could occur on the coupon surface under Cl⁻ conditions. Meanwhile, Mo ions will appear in the initial corrosion product. With prolonged corrosion time, one Mn(II) replaces one Fe(II) in the octahedral centre of Fe₃O₄ crystal [18]. MoO₄²⁻ produced simultaneously can reduce anion permeability of the rust film; however, according to the Fe-Mn potential-pH diagram, most of the MnFe₂O₄ region did not overlap with the Fe₃O₄ region. It is assumed that progressively more anode ions appear in the corrosion products, reducing the electronegativity of the crystal. Therefore, the rust films will not effectively block the penetration of chloride ions when Mn ions are present. In the later stage of corrosion, Mn ions, which appeared earlier when corrosion was stable, migrated along the rust film. The MnFe₂O₄ gradually turned into relatively stable Mn₃O₄; therefore, the Mn-rich compound began to appear in the external rust film, and gradually gathered in the central rust layer.

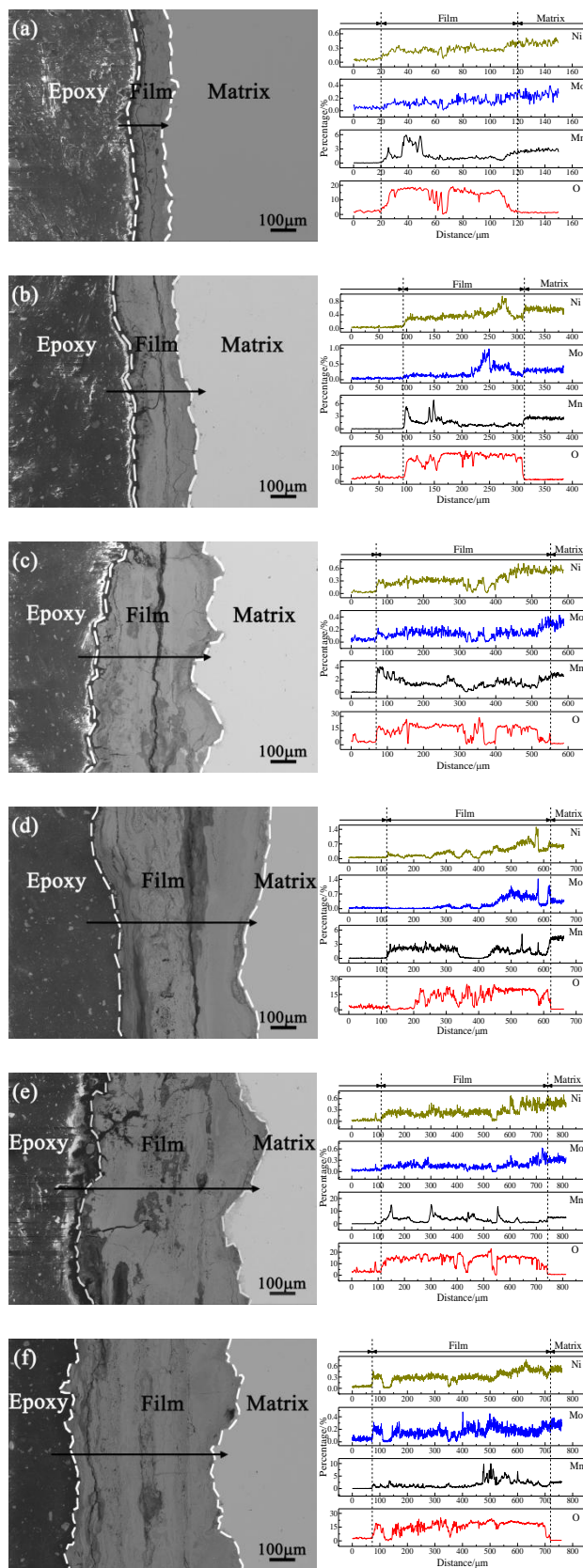


Figure 8. Cross section of the Mn-Mo-Ni steel and the main element distribution in the corrosion products film in a simulated seawater environment at 25 °C for different lengths of time: (a) 24 h; (b) 72 h; (c) 168 h; (d) 288 h; (e) 432 h; (f) 600 h. Each corrosion cycle consisted of a 10 mins wetting period in 3.5 (mass. %) NaCl solution plus a 50 mins drying period.

The Mn-Mo-Ni steel corrosion processes were similar to those of Mn-Mo steel except that Mo and Ni may cooperatively influence Mn ions during the corrosion process. The volatility ranges of Mo and Ni were similar (Fig. 8). Whereas the role of Mo was selective cation permeability, the role of Ni in the entire corrosion process was to evenly distribute the corrosion productions; the function of Ni in promoting the precipitation of α -FeOOH was unclear due to its low concentration.

4. CONCLUSIONS

The influences of Mn on corrosion behaviour in a simulated seawater environment by cyclic wet/dry corrosion tests have been expounded. The following conclusions can be drawn from this work:

(1) The Mn content in medium manganese steel can impact the corrosion rate of the steel.

(2) The two tested medium manganese steels had different corrosion behaviour, namely in the distribution of the corrosion products. $MnFe_2O_4$ produced by Mn and FeOOH may increase the precipitation of cations in the corrosion product.

(3) The effects of alloying Mo and Ni on the accelerated corrosion behaviour of Mn element were different. The formation of Mo oxides can effectively control the selective cation permeability of the element due to the influence of Mn. Because of its low concentration, the function of Ni in promoting the precipitation of α -FeOOH was not to improve the extent of corrosion.

ACKNOWLEDGEMENT

This work was financially supported by the National High-tech R&D Program (863 Program) No.2015AA03A501.

References

1. M. Stratmann, K. Bohnenkamp, T. Ramchandran, *Corros. Sci.*, 27 (1987) 905-926.
2. N.W. Dai, J.X. Zhang, Q.M. Chen, B. Yi, F.H. Cao, J.Q. Zhang, *Corros. Sci.*, 99 (2015) 295-303.
3. T. Misawa, K. Asami, K. Shimodaira, *Corros. Sci.*, 14 (1974) 279-289.
4. R.E. Melchers, *Corros. Sci.*, 46 (2004) 1669-1691.
5. Ph. Refait, A.-M. Grolleau, M. Jeannin, E. François, R. Sabot, *Corros. Sci.*, 111 (2016) 583-595.
6. M. Reffass, R. Sabot, C. Savall, *Corros. Sci.*, 48 (2006) 709-726.
7. M. Itagaki, R. Nozue, K. Watanabe, H. Katayama, K. Noda, *Corros. Sci.*, 46 (2004) 1301-1310.
8. M.E. E-Perez, J. P-Calderon, E. V-Velez, M. C-Diaz, J.G. G-Rodriguez, L. M-Gomez, *Int. J. Electrochem. Sci.*, 11 (2016) 374-384.
9. Q.C. Zhang, J.S. Wu, J.J. Wang, W.L. Zheng, J.G. Chen, A.B. Li, *Mater. Chem. Phys.*, 77 (2003) 603-608.
10. C. Wen, Y.W. Tian, G. Wang, J.Z. Hu, P.C. Deng, *Int. J. Electrochem. Sci.*, 11 (2016) 4161-4173.
11. Y.H. Qian, C.H. Ma, D. Niu, J.J. Xu, M.S. Li, *Corros. Sci.*, 74 (2013) 424-429.
12. I. Diaz, H. Cano, D. de la Fuente, B. Chico, J.M. Vega, M. Morcillo, *Corros. Sci.*, 76 (2013) 348-360.
13. M. Kimura, H. Kihira, N. Ohta, M. Hashimoto, T. Senuma, *Corros. Sci.*, 47 (2005) 2499-2509.
14. L. Bousselmi, C. Fiaud, B. Tribollet, E. Triki, *Corros. Sci.*, 39 (1997) 1711-1724.
15. Y.S. Choi, J.J. Shim, J.G. Kim, *J. Alloys Compd.*, 391 (2005) 162-169.
16. B.W. Forgeson, C.R. Southwell, A.L. Alexander, *Corrosion*, 16 (1960) 87-96.

17. W.A. Schultze, C.J. van der Wekken, *Br. Corros. J.*, 11 (1976) 18–24.
18. L. Hao, S.X. Zhang, J.H. Dong, W. Ke, *Corros. Sci.*, 53 (2011) 4187-4192.
19. ASTM Standard G1-03, *ASTM International*, West Conshohocken, PA, USA.
20. K. Asami, M. Kikuchi, *Corros. Sci.*, 45 (2003) 2671-2688.
21. A. Raman, S. Nasrazadani, L. Sharma, *Metallography*, 22 (1989) 79-96.
22. Bijayani Panda, R. Balasubramaniam, Gopal Dwivedi, *Corros. Sci.*, 50 (2008) 1684-1692.
23. T. Kamimura, S. Hara, H. Miyuki, M. Yamashita, H. Uchida, *Corros. Sci.*, 48 (2006) 2799-2812.
24. R. Balasubramaniam, A.V. Ramesh Kumar, P. Dillmann, *Curr. Sci.*, 85 (2003) 1546-1554.
25. W. Meisel, *J. Phys. Colloq.*, 41.C1 (1980) C1-63-C1-70.
26. R. Wang, S. Luo, M. Liu, Y. Xue, *Corros. Sci.*, 85 (2014) 270-279.
27. W.Y. Lv, C. Pan, W. Su, Z.Y. Wang, S.N. Liu, C. Wang, *J. Mater. Eng. Perform.*, 24 (2015) 2597-2604.
28. H. Krawiec, V. Vignal, O. Heintz, R. Oltra, *Electrochim. Acta*, 51 (2006) 3235-3243.
29. I.-u.-H. Toor, *Int. J. Mater. Res.*, 105 (2014) 386-391.
30. I.-u.-H. Toor, *J. Chem.-NY.*, 2014 (2014) 1-8.
31. M.P. Ryan, D.E. Williams, R.J. Chater, B.M. Hutton, D.S. McPhail, *Nature*, 415 (2002) 770-774.
32. K.L. Chao, H.Y. Liao, J.J. SHyue, S.S. Lian, *Metall. Mater. Trans.*, B 45 (2014) 381-391.
33. X.Q. Wu, S. Xu, J.B. Huang, E.H. Han, W. Ke, K. Yang, Z.H. Jiang, *Mater. Corros.*, 59 (2008) 676-684.
34. Y.L. Zhou, J. Chen, Y. Xu, Z.Y. Liu, *J. Mater. Sci. Technol.*, 29 (2013) 168-174.
35. S.-K. Kwon, K. Shinoda, S. Suzuki, Y. Waseda, *Corros. Sci.*, 49 (2007) 1513-1526.
36. B. Beverskog, I. Puigdomenech, *Corros. Sci.*, 38 (1996) 2121-2135.
37. Y. Marcus, Ion properties, *Marcel Dekker, Inc.*, New York, 1997.